Ultramicroscopy 111 (2010) 47–55

Contents lists available at ScienceDirect

Ultramicroscopy

journal homepage: www.elsevier.com/locate/ultramic

Precession electron diffraction using a digital sampling method

Daliang Zhang [a,b], Daniel Grüner [a], Peter Oleynikov [a], Wei Wan [a], Sven Hovmöller [a,*], Xiaodong Zou [a]

[a] Inorganic and Structural Chemistry and Berzelii Center EXSELENT on Porous Materials, Department of Materials and Environmental Chemistry, Arrhenius Laboratory, Stockholm University, SE-106 91 Stockholm, Sweden
[b] State Key Laboratory of Inorganic Synthesis and Preparative Chemistry, Jilin University, Changchun 130012, China

ARTICLE INFO

Article history:
Received 22 April 2010
Received in revised form
17 September 2010
Accepted 21 September 2010

Keywords:
Precession electron diffraction
Crystallography
Data processing
Crystal structure
TEM control
Lorentz correction

ABSTRACT

A software-based method for collecting precession electron diffraction (PED) patterns is described. The PED patterns are obtained on a computer controlled transmission electron microscope. A series of electron diffraction (ED) patterns are collected as still ED frames at equal intervals, while the electron beam is precessed by one period (360°) around the optical axis. A PED pattern is obtained by combining the different ED frames, which resembles the sampling of a conventional PED pattern. Since intermediate ED frames are collected, it is possible to perform different post-processing strategies on the ED data. This can be used for geometric corrections to obtain accurate integrated intensities. The alignments and data collection are fully automated and controlled by software. The data quality is comparable to what can be achieved using specialized hardware for precession. The PED data can be used for structure solution and refinement with reasonably good *R*-values.

1. Introduction

After Vincent and Midgley first described precession electron diffraction (PED) in 1994 [1], a few laboratories built their own devices for PED [2–4]. It was only when a commercial precession unit was made available by NanoMEGAS ("Spinning Star") in 2004 [5] that the method became widely spread. Today PED is performed in dozens of laboratories world-wide. In a PED data collection, the electron beam is tilted off the optical axis by a precession angle φ and precessed with an angle ω around the optical axis on the surface of a cone (Fig. 1), where one period of precession corresponds to ω from 0° to 360°. After passing through the specimen, the electron beam is tilted back, so that the direct beam coincides with the optical axis (de-scan). With the PED method, dynamical effects may be reduced, because only a few reflections are in Bragg condition simultaneously. The intensity data can then be treated within the kinematical approximation, which makes all the structure solution methods developed for the X-ray diffraction, such as the direct methods, Patterson method and charge flipping available also for electron diffraction. The PED technique has been successfully applied to a number of structural studies [6–15]. It also showed great benefits for crystal symmetry determination [16,17].

In a conventional, hardware precession system such as the "Spinning Star", the TEM coils used for controlling the electron beam are controlled by a dedicated external electronic device, which provides simultaneous and continuous signals for beam tilt and de-scan. During the electron beam precession, the Ewald sphere scans through every reflection, with different excitation errors s depending on ω (Fig. 2). The final PED pattern is a continuous integration of the reflections over the entire range of ω. In general, this integration is repeated several precession periods, because a typical exposure time is much longer than the time of each precession period. Information about the shape of the reflections is lost by integrating over ω; the PED pattern contains only the integrated intensities. Furthermore, in a PED pattern, reflections at low angle stay in Bragg condition for longer time than those at high angles. This leads to a geometrical error in PED patterns, the so-called Lorentz effect that needs to be corrected for. Correction factors for Lorentz effect have been proposed [1,18].

CCD cameras and modern electron microscopes are computer-controlled, offering interfaces to write programs and to do scripting. It is thus possible to collect electron precession diffraction patterns by software and to automate all necessary alignment procedures. The prospect of developing a precession electron diffraction program has been discussed [19]. To our knowledge, the first implementation of software-based PED was reported only recently [20]. One of the most important advantages of the software-based PED is that no dedicated PED hardware is needed to be attached to the TEMs, which makes the installation easier and free of possible interference with other TEM functions. Although data collection based on software is slower than hardware precession with dedicated electronics to control the TEM coils, software-based PED data collection with automatic alignment procedures will save

* Corresponding author. Tel.: +46 8 16 23 80; fax: +46 8 16 31 18.
E-mail address: sven.hovmoller@mmk.su.se (S. Hovmöller).

0304-3991/$ - see front matter © 2010 Elsevier B.V. All rights reserved.
doi:10.1016/j.ultramic.2010.09.008

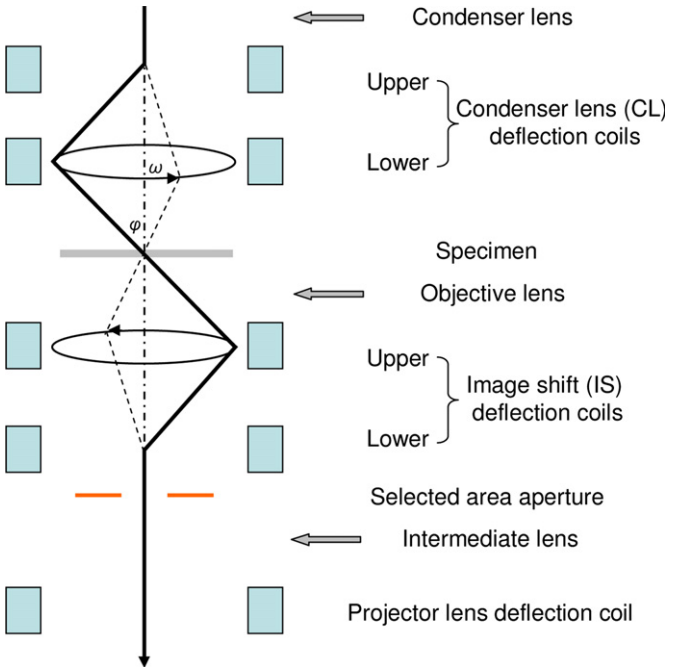

Fig. 1. Schematic diagram of the electron beam path for precession electron diffraction in a TEM.

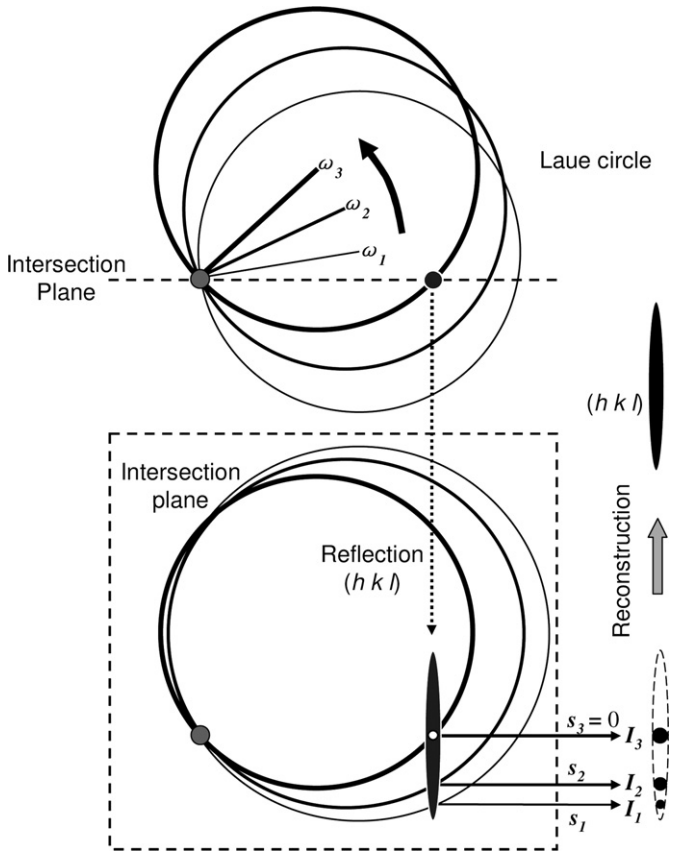

Fig. 2. Schematic representation of the sampling method. The Laue circles of three consecutive electron beam tilts (ω_1, ω_2 and ω_3) are indicated by thin, intermediate and thick circles, respectively. (Above) The three Laue circles together with the direct beam and a reflection ($h\,k\,l$) viewed both along the optical axis. (Below) An intersection perpendicular to the optical axis containing the direct beam and the reflection ($h\,k\,l$). In the intersection plane, the radii of the intersection circles of the Ewald sphere are different, depending on the angle ω. Different diffraction intensities, I, are observed when the Ewald sphere intercepts the reflection at different values of the excitation errors. A profile of the reflection ($h\,k\,l$) can be reconstructed by combining the observed intensities and the corresponding excitation errors.

a large amount of user's interactions and time in the alignment and fine-tuning. Software-based precession also has other advantages that will be discussed in this article. Here, we introduce a sampling method for software-based PED data collection and propose data post-processing procedures for Lorentz correction.

2. Experimental

Crystals of $K_2O \cdot 7Nb_2O_5$ (space group $P4/mbm$ (No. 127), $a=b=27.5$ Å, $c=3.94$ Å), which are stable under the electron beam, were used as a test sample for data collection. The crystal structure was determined by HRTEM [21]. Recently, we showed that the structure could also be solved by direct methods from the PED data recorded by the Spinning Star precession unit [22]. The crystal structure of an isotypic compound, $Tl_2O \cdot 7Nb_2O_5$, was solved by X-ray crystallography [23].

A small amount of $K_2O \cdot 7Nb_2O_5$ crystals was crushed in an agate mortar and dispersed in ethanol. After ultrasonic treatment, a drop was taken from the dispersion and transferred to a copper grid covered with a holey carbon film.

PED data were collected on a JEOL JEM2100 TEM operated at 200 kV. The diffraction patterns were recorded using either an upper mounted Gatan ES500W Erlangshen camera or a bottom mounted Gatan SC1000 ORIUS CCD camera. A series of 120 ED frames was recorded by changing the angle ω in steps of 3°. PED data were post-processed by a program written in DigitalMicrograph script. Intensities of reflections were extracted from raw- or post-processed diffraction patterns using the programs ELD [24] and analyzed by Triple [25]. Structure solution and refinement were performed, using the program SHELX-97 [26]. Starting values for the atomic positions were taken from the crystal structure of $Tl_2O \cdot 7Nb_2O_5$ [23]. Because refinements of oxygen and potassium positions were not stable and resulted in unreasonable atomic positions, only the positions of Nb atoms were refined, whereas positions of O and K atoms were kept fixed. In addition, isotropic displacement parameters were refined and constrained to be identical for each element. In total, 17 parameters were refined using two-dimensional data sets containing 305 unique reflections up to 1.0 Å resolution. Kinematically forbidden reflections ($h00$: $h=2n+1$; $0k0$: $k=2n+1$), which are observed in the PED patterns, were excluded. The quality of the PED data was evaluated by calculating the R factor for merging symmetry equivalent reflections, R_{merge}, using the program SHELX-97 [26]

$$R_{\mathrm{merge}} = \frac{\sum_{hk}\left|F_o^2(hk0) - F_{\mathrm{sym}}^2(hk0)\right|}{\sum_{hk}F_o^2(hk0)} \quad (1)$$

Both summations in Eq. (1) involve only those reflections for which symmetry equivalents are present in the data set. The high (tetragonal) symmetry of the crystal, in combination with the large unit cell parameter a (27.5 Å), which results in a large number of reflections in a [0 0 1] zone axis pattern, is very useful for this purpose. Because most of the reflections were very weak and relatively unreliable in the region beyond 1 Å resolution, only reflections within 1 Å resolution (2315 reflections in total, of which 305 unique) were used in the calculations of R_{merge} and for the structure refinement. The standard deviations of integrated intensities, $\sigma(I)$, were estimated to be 1% of the intensity of the strongest reflection. Two indicators $R1$ and $\langle \Delta r \rangle$ were used to judge the

quality of the structure refinement

$$R1 = \frac{\sum \left||F_o|-|F_c|\right|}{\sum |F_o|} \quad (2)$$

and

$$\langle \Delta r \rangle = \frac{1}{N}\sum_{N} |r_{\text{refined}} - r_{\text{reference}}| \quad (3)$$

where $\langle \Delta r \rangle$ is the average shift of the framework Nb atom positions r_{refined} with respect to the positions $r_{\text{reference}}$ in the reference structure ($Tl_2O \cdot 7Nb_2O_5$). In the present case, there are $N=7$ framework Nb atoms with refinable positions.

3. Description of the digital sampling method

3.1. The sampling method

Rather than the continuous electron beam precession achieved by conventional precession units, in the digital sampling method the beam is moved around in a circle with constant steps in sufficiently many discrete points. This is possible with computer-controlled TEMs. During data collection by the digital sampling method, the electron beam is precessed around the optical axis in discrete angles ω_i, where $0^\circ \le \omega_i < 360^\circ$ (Fig. 1). For each ω_i, an ED frame is recorded and stored. A full PED pattern is obtained by adding up all the ED frames. If the number of ED frames is large enough, this summed ED pattern is essentially identical to a conventional PED pattern. In addition, the ED frames contain more valuable information than a single PED pattern, since each reflection is intercepted by the Ewald sphere at different excitation errors by a series of consecutive ED frames as shown schematically in Fig. 2. This allows us to extract information on the reflection intensity profiles and to implement post-processing procedures to correct for Lorentz effect, so that accurate diffraction intensities can be obtained.

3.2. Electron beam path

The electron beam path for the digital precession electron diffraction is shown in Fig. 1. The electron beam is controlled by the condenser lens (CL) deflection coils and the image shift (IS) deflection coils. First, the electron beam is tilted by a pair of CL deflection coils using the beam tilt function in a TEM, which is often used for recording dark field images. An upper CL deflection coil tilts the electron beam off the optical axis by an angle of φ. This moves the electron beam away from the crystal. A lower CL deflection coil then brings the electron beam back to the same position of the crystal by applying an angle of -2φ. The upper and lower CL deflection coils are combined so that the electron beam remains stationary on the crystal as the electron beam is tilted and precessed.

Below the specimen, the direct beam is thus off the optical axis by $-\varphi$ and will move as the electron beam is precessed. To make the direct beam stationary at the recording media (for example a CCD camera), we must use extra deflection coils below the specimen to compensate for the displacement, i.e. to de-scan the electron beam. There are two choices for the de-scan: by using IS deflection coils or using the projector lens deflection coils. We choose IS deflection coils, because they are placed above the intermediate lenses, so that the de-scan settings will be independent of the camera length. Two IS deflection coils (upper and lower) are combined to de-scan the direct beam. The upper IS deflection coil deflects the direct beam by 2φ towards the optical axis of the TEM and finally the lower IS deflection coil tilts the electron beam by $-\varphi$ back onto the optical axis, so that the direct beam stays at the same position on the CCD camera in the diffraction mode.

3.3. Description of the alignment and data collection procedure

The important criteria for precession electron diffraction are that (1) the electron beam should precess in a strictly conical way around the optical axis with constant precession angle, and remain at the same position of the crystal; (2) after the de-scan, the direct beam should go along the optical axis and stay at the same position in every ED frame. The PED data are collected fully automatically by a software that controls the CL and IS deflection coils as well as the CCD camera. Prior to data acquisition, all the deflection coils must be aligned, which is done by the software using an automatic alignment procedure. In addition, the precession angle and the CL deflection coils also need to be calibrated in advance at each accelerating voltage. The following steps are needed; they are described in detail below. The procedure is schematically summarized in a flow chart in Fig. 3.

3.3.1. Initial TEM alignment

Initial TEM alignment needs to be done according to the instructions from the manufacturer of the TEM. The alignments

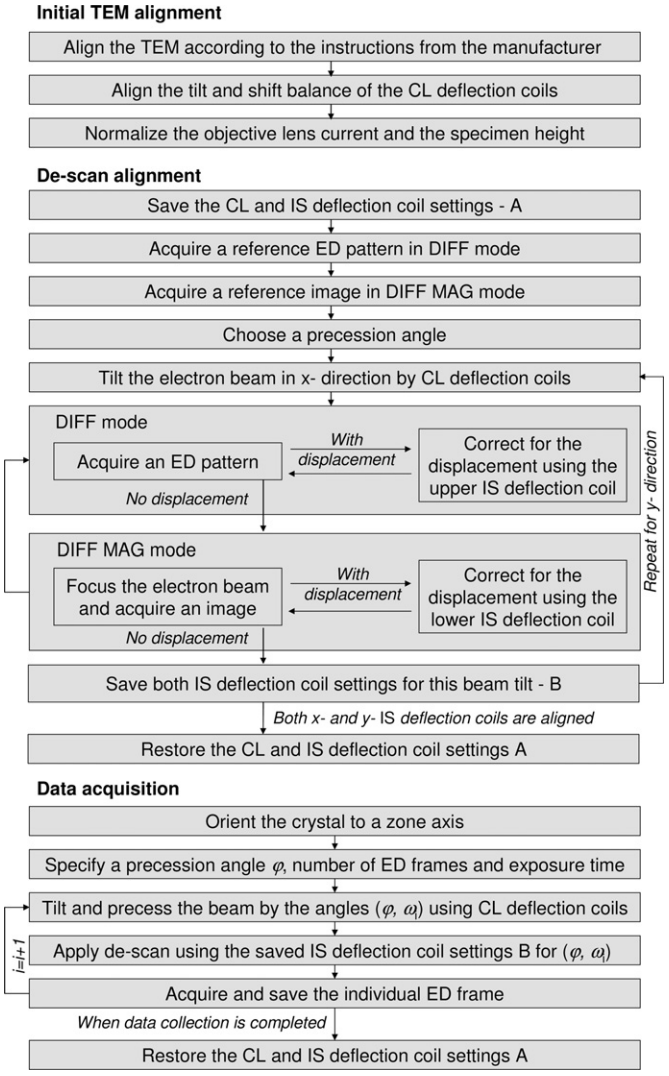

Fig. 3. Flow chart of the automatic digital PED alignment and data acquisition procedure.

of the tilt and shift balances of the CL deflection coils are especially important, since they control whether the same area of the crystal is illuminated during the electron beam precession. The objective lens current should be adjusted to its optimum value and the sample should be placed at the eucentric height.

3.3.2. Automatic de-scan alignment

The de-scan is performed by the IS deflection coils below the specimen. These IS deflection coils should synchronize with the CL deflection coils above the specimen, so that the direct beam always remains at the same position on the detector during the electron precession. The IS deflection coils influence the electron beam in both image and diffraction modes. Misalignment of a deflection coil results in a movement of the electron beam in diffraction and/or image mode. These movements are measured by calculating the cross-correlation of the ED frames or images with and without applying the electron precession, and subsequently corrected by the IS deflection coils. The alignment of the IS deflection coils is done in both diffraction and image modes. First the upper IS deflection is aligned in the diffraction mode (DIFF), and then the lower IS deflection coil is aligned in an image mode (DIFF MAG). When the lower IS deflection coil is aligned in an image mode, displacements of the electron beam show up in the diffraction mode. The alignment in diffraction and image mode is iterated until the electron beam remains at the same positions in both diffraction and image modes (Fig. 3). Only a few iterations are often enough for such an alignment. Because each deflection coil is composed of *x*- and *y*-deflectors, the alignment needs to be done on both *x*- and *y*-directions, with $\omega=0^\circ$ and 90°, respectively. The beam tilt in any other direction is obtained by combining the *x*- and *y*-deflectors. The settings for the IS defection coils are saved and can be reloaded. The de-scan alignment is done automatically by the software and one such alignment is often enough throughout each TEM session.

3.3.3. Calibration of the precession angle and the CL deflection coils

The precession angle, i.e. the tilt angle of the electron beam generated by the CL deflection coils, has to be calibrated. This is done without the de-scan by measuring the displacement of the direct beam on the diffraction pattern of a standard powder sample, for example, Al or Au powder. Based on our tests, it suffices to calibrate a small number of beam tilts and interpolate for other angles. The precession angle (φ) is calculated from the direct beam shift R_{beam} and the radii of a powder ring R_{ring} in the diffraction pattern using the following equation: $\sin\phi/\sin 2\theta = R_{\mathrm{beam}}/R_{\mathrm{ring}}$, where θ is the Bragg angle for the powder ring and can be calculated from the corresponding *d*-value of the powder ring and the electron wavelength using the Bragg equation: $2d\sin\theta=\lambda$. The calibration of the CL deflection coils needs to be done on both *x*- and *y*-directions, and for each accelerating voltage.

It is important to ensure that the beam tilt angle is exactly the same in *x*- and *y*-directions so that the electron beam precesses in a strictly conical way to generate a perfect circle on the CCD camera in the diffraction mode. The settings are saved and just need to be reloaded for data acquisition.

3.3.4. Data acquisition

Before data acquisition, one should make sure that the above mentioned alignment and calibration have been done. A thin crystal should be selected and oriented with a certain zone axis exactly parallel to the optical axis. The objective lens current should be adjusted to its optimum value. The specimen should be placed at the eucentric height.

As shown in Fig. 3, the user should specify a precession angle (φ), the number of ED frames (N) and an exposure time for the data collection. The precession step ($\Delta\omega$) is determined by N, as $\Delta\omega=360^\circ/N$. To collect an ED frame i, the electron beam is tilted off the optical axis by φ and precessed around the optical axis by $\omega_{\mathrm{i}}=(i-1)\cdot\Delta\omega$, using the CL deflection coils and the corresponding pre-saved settings. Below the specimen, the electron beam is de-scanned by the IS deflection coils according to the pre-saved settings. Then, an individual ED frame is recorded using a CCD camera, before proceeding to the next angle $\omega_{\mathrm{i}+1}$. At each step, an ED frame is obtained and stored. The data collection time of the software-based electron precession diffraction depends on the exposure time, the number of ED frames and the speed of the CCD camera. In our case, we used 0.1–0.5 s exposure time for the individual ED frames, which resulted in a total acquisition time of 20–60 s for collecting one full PED data set, composed of 120 ED frames.

3.4. Data processing

3.4.1. sum-PED

If all the alignments are done properly, the direct beam of all ED frames should share the same position. Then, all the ED frames can be simply added up to get a combined diffraction pattern, which is equivalent to a conventional PED pattern and is designated *sum*-PED in the following. Our data showed that the positions of the direct beam on different ED frames within each series differ by 1–2 pixels (with a standard deviation of one pixel), which makes the summation possible. Otherwise the individual ED frames have to be aligned with the common direct beam before they are added together.

3.4.2. Lorentz corrected sum-PED

Lorentz effect on PED is purely geometric, in an analogy with similar effects due to the geometry and data collection procedure in the X-ray diffraction. This effect results in different number of sampling points for low and high angle reflections, which leads to systematically enhanced intensities of low-angle reflections in both conventional and *sum*-PED, as will be discussed in Section 4.1. The intensities corrected for the Lorentz effect, I_{corr}, are calculated from the intensities summed over all ED frames I_{sum}, according to the analytical expression proposed by Gjønnes [18]

$$I_{\mathrm{corr}}(hk0)=\frac{R_0 g\sqrt{1-(g/2R_0)^2}}{2K}I_{\mathrm{sum}}(hk0) \tag{4}$$

where R_0 is the radius of the Laue circle ($K\bullet\sin(\varphi)$ with precession angle φ), g is the length of the scattering vector of the reflection ($h\,k\,0$), and K is the length of the incident electron wave vector.

3.4.3. max-PED

We have implemented a *max* function, where the intensity at each pixel in the final PED (*max*-PED) pattern represents the highest value for this particular pixel among all the ED frames. A *max*-PED pattern contains an intensity from each reflection, when it is very close to or at an exact Bragg condition. The *max*-PED is basically free of Lorentz effect, because we only consider the highest intensity of the series of measurements for a reflection.

3.4.4. integrated-PED

Once the orientation of the incident electron beam has been perfectly aligned along a certain zone axis of the specimen, the position and radius of the Laue circle can be calculated for the ED frames. Only reflections exactly on the Laue circle are in the exact Bragg condition. However, each reflection is extended in reciprocal space, and will contribute scattered intensity even if it slightly deviates from the exact Bragg condition with a so-called excitation error *s*. The excitation error is defined to be negative, if a reflection

is inside the Ewald sphere and positive if it is outside. Excitation errors of all reflections on each ED frame can be estimated. This allows us to plot the intensity profile of any given reflection, as a function of the excitation error, i.e. a rocking curve, from a series of ED frames, as is done in Fig. 5.

Integrated intensities are equal to the area under the intensity profile of a reflection along the excitation error. Thus, different numbers of sampling points for low and high angle reflections will not affect the integrated intensity, i.e. *integrated*-PED patterns are free from Lorentz effects. An *integrated*-PED pattern is obtained by first calculating the excitation error for each pixel in every ED frame, and then integrating the intensity profile for each pixel as follows:

$$I_{\text{pixel}}^{\text{integrated}} = \sum_{i=1}^{N-1} \frac{I_{\text{pixel},\ i} + I_{\text{pixel},\ (i+1)}}{2} |s_i - s_{i+1}| \tag{5}$$

where s is the excitation error (in Å^{-1}), N is the number of ED frames and i is the frame index.

4. Results and discussion

4.1. Example: PED at a precession angle of 1.1°

A set of PED data was collected using the sampling method with a precession angle of 1.1°. A PED data set collected with 120 ED frames is shown in Fig. 4. A [0 0 1] zone axis was found on a thin specimen of $K_2O \cdot 7Nb_2O_5$ and the crystal was well aligned before starting the data collection program (Fig. 4a). When the data collection started, the electron beam was tilted away from the optical axis of the TEM by the precession angle of 1.1° and an ED frame was recorded (Fig. 4b). Then, another ED frame is obtained by precessing the electron beam around the optical axis by $\Delta\omega$, which equals to a precession step of 3°. After a number of ED frames have been collected, a partial combined pattern can be obtained by adding the individual ED frames (Fig. 4c). When the electron beam has been precessed by the full circle of 360°, the data collection is completed and a final combined pattern, *sum*-PED, is obtained (Fig. 4d).

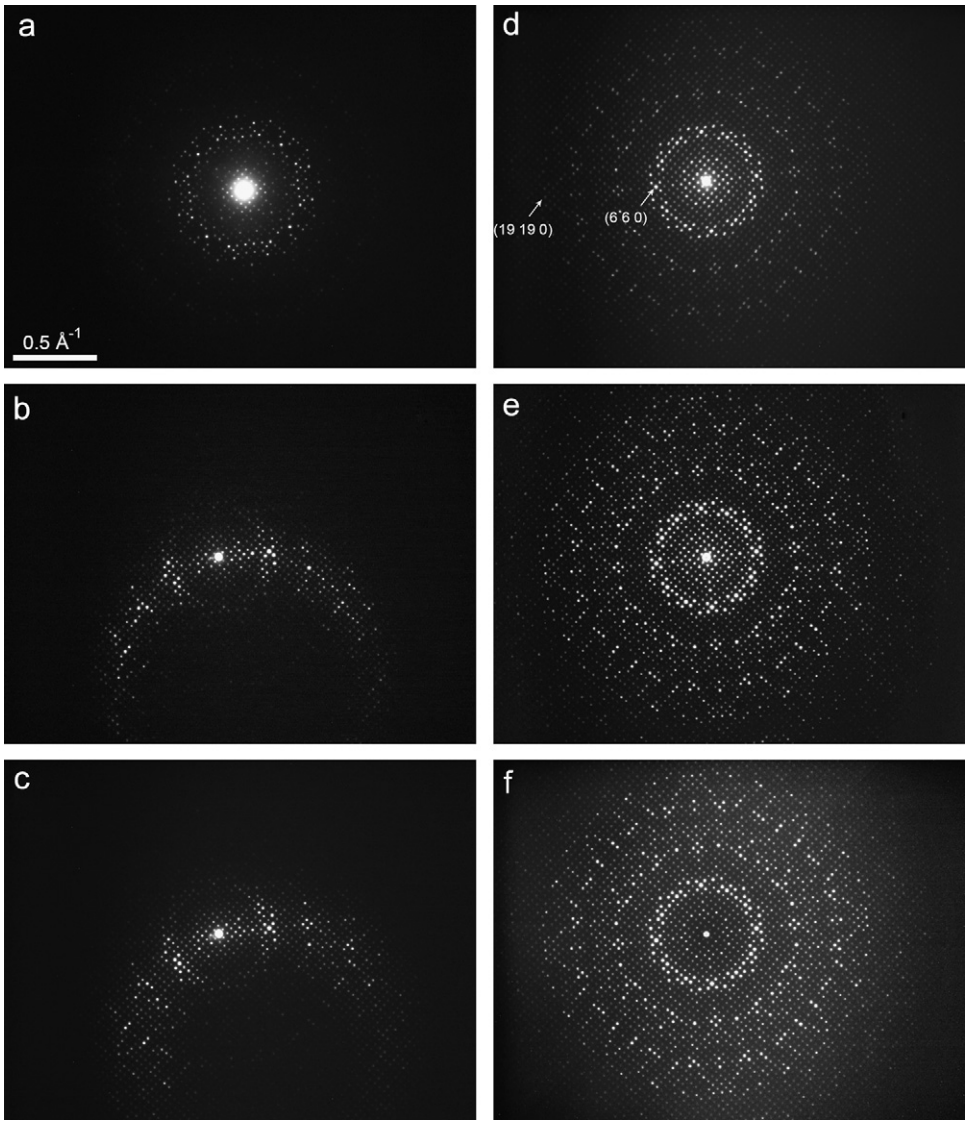

Fig. 4. (a) SAED pattern taken from a thin specimen of $K_2O \cdot 7Nb_2O_5$; (b) a single ED frame taken from the same specimen as the SAED pattern shown in (a); (c) a combined ED pattern by summation of ten consecutive ED frames; (d) *sum*-PED pattern by summation of all 120 ED frames. Two reflections (6 6 0) (d=3.24 Å) and (19 19 0) (d=1.02 Å) are marked; (e) *max*-PED pattern obtained by using the maximum intensity values at each pixel, from all individual ED frames; (f) *integrated*-PED pattern by integrating the intensity over the excitation errors. High angle reflections in (e) and (f) show higher intensity compared to those in the *sum*-PED pattern, because the geometrical distortions have been corrected. (c), (d), (e) and (f) are collected with a precession angle of 1.1° and a precession step of 3°. 120 ED frames are recorded in total.

In Fig. 4b, the Laue circle is clearly seen. The calculated values of the excitation error for the ED frame in Fig. 4b are shown in Fig. 5a. The inner white circle, passing through the direct beam, indicates the Laue circle, where the excitation error is equal to zero. The outer circle indicates an excitation error of 0.008 $Å^{-1}$. These two circles share the same origin, where the excitation error has its minimum value, -0.008 $Å^{-1}$.

The rocking curves of the (6 6 0) and (19 19 0) reflections ($d_{(6\,6\,0)}$=3.24 Å, $d_{(19\,19\,0)}$=1.02 Å) marked in Fig. 4d are shown in Fig. 5b and c, respectively. The reflection (19 19 0) is 0.98 $Å^{-1}$ away from the (0 0 0) reflection. This is approximately three times as far as (6 6 0) which is at 0.31 $Å^{-1}$. Thus, the Ewald sphere sweeps through (19 19 0) about three times faster than through (6 6 0). Thus, there are less sampling points across the peak (19 19 0). In other words, there are less ED frames that contain an intensity from the (19 19 0) reflection compared to the (6 6 0) reflection. This introduces a systematic error in the *sum*-PED pattern. Once rocking curves of all reflections are known, this systematic error can be corrected by post processing according to one of the following two approaches, *max*-PED and *integrated*-PED defined in Section 3.4.

The PED data set shown in Fig. 4 is treated with the *max* function to produce a so-called *max*-PED pattern. Compared to the *sum*-PED pattern (Fig. 4d), the *max*-PED data (Fig. 4e) shows much higher signal-to-noise ratio. The relative intensities of the high angle reflections are increased compared to *sum*-PED data, and many high angle reflections that are invisible in the *sum*-PED pattern become visible in a *max*-PED pattern. The *integrated*-PED pattern (Fig. 4f) looks very similar to the *max*-PED pattern, but both are distinctly different from the *sum*-PED.

4.2. Number of ED frames

The number of ED frames needed depends on the peak widths and the resolution of the reflections at the highest diffraction angle (compare Fig. 5b and c). In order to sample a peak, at least three sampling points are recorded within the full width at half maximum (FWHM) of the peak. The intensity curve of the (19 19 0) reflection as a function of excitation error *s* obtained from 120 ED frames contains three sampling points above half the maximum peak height (Fig. 5c). Thus, here, 120 ED frames are sufficient to get

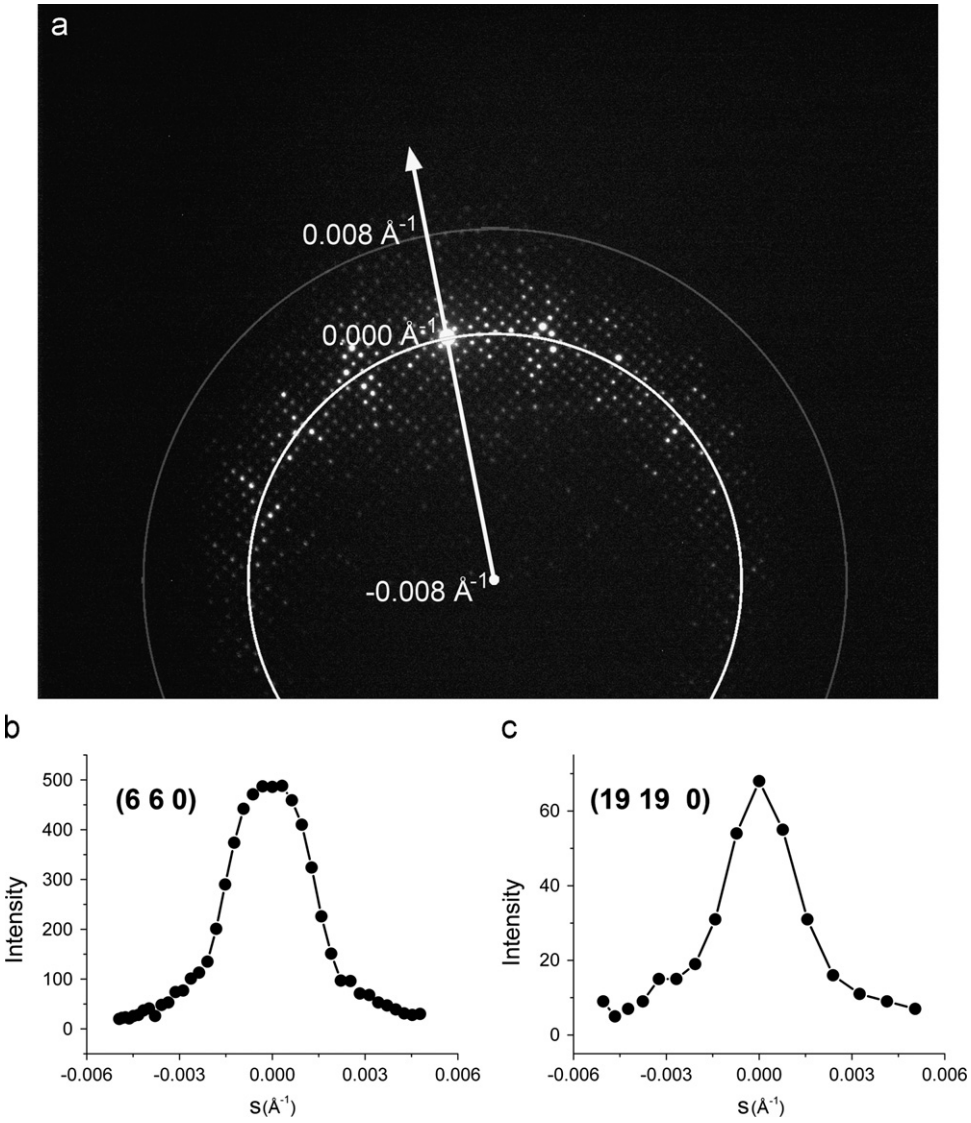

Fig. 5. (a) An ED frame with the estimated excitation errors marked. The frame is the same as in Fig. 4b. (b) and (c) Intensity profiles of the (6 6 0) and (19 19 0) reflections (marked in Fig. 4d), as a function of an excitation error *s*. The black dots show how the profiles are sampled. The profile in (b) has three times more sampling points than that in (c).

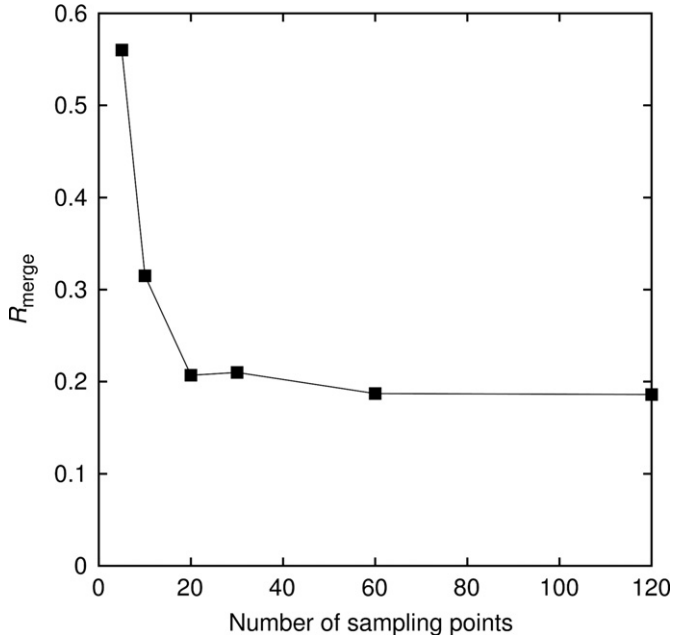

Fig. 6. The influence of the number of ED frames on the *R* value for merging symmetry-equivalent reflections, R_{merge}, for an *integrated*-PED pattern recorded at 1.1° precession angle.

enough sampling points on a reflection with *d*-spacing close to 1 Å. If there are less sampling points, the reflection profile will be too poorly defined for an accurate intensity integration. The width of the reflections depends on crystal thickness and other factors. If only data to lower resolution are to be collected, for example 3.24 Å as the (6 6 0) reflection, then a smaller number (40) of ED frames would be enough to get three sampling points above half the maximum peak.

The effect of the number of ED frames can be judged by extracting the integrated intensities for all reflections present in the PED pattern, and then calculating the *R* value for merging symmetry-equivalent reflections, R_{merge}. This approach is particularly justified when only the integrated intensities are of interest, e.g. for solving and refining crystal structures. If a detailed reconstruction of reciprocal space is needed, a finer precession step width is desirable to get more ED frames. An insufficient number of ED frames leads to an increased R_{merge}, because different but symmetry-equivalent reflections are intersected differently by the Ewald sphere. In the present study, R_{merge} did not decrease much when more than 20 ED frames were used, as seen in Fig. 6. The *integrated*-PED pattern obtained using 20 ED frames displays only small deviations from the 4*mm* symmetry. Using 120 rather than 60 ED frames did not improve the data quality significantly. For thicker crystals and if data resolution considerably higher than 1 Å resolution is aimed at, it may be necessary to collect 120 or even more ED frames.

4.3. integrated-PED: correction of Lorentz effect

As described in Section 4.1, the Lorentz effect leads to systematically enhanced intensities of low-angle reflections, if the intensities are just summed up (*sum*-PED or conventional PED). Our approach to Lorentz correction is rather fundamental: the sampling rate problem is circumvented by taking the step size between sampling points into account—for each individual pixel. Although analytical expressions for the Lorentz correction have been proposed for correction of integrated intensity data [18], the correction sometimes resulted in poor intensity data for structure determination [6]. With the sampling method, both the corrected (*integrated*-PED) and the uncorrected (*sum*-PED) data are available, so we can derive the Lorentz correction factor from experimental data by dividing the integrated intensities of reflections extracted from *sum*-PED and *integrated*-PED patterns, as shown in Fig. 7. The ratio of integrated intensity extracted from *sum*-PED and *integrated*-PED patterns matches the correction function (Eq. (4)) proposed by Gjønnes [18] very well. On the other hand, as has been discussed in Section 4.2, a sufficient number of sampling points is significant for the calculation of *integrated*-PED.

4.4. Comparison of sum-, Lorentz corrected sum-, max- and integrated-PED data

In order to obtain a quantitative measure for data quality, *sum*-PED, *max*-PED and *integrated*-PED patterns were processed. Intensities were extracted from each of the PED patterns using ELD [24], and used for the structure refinement of $K_2O \cdot 7Nb_2O_5$. In addition, a Lorentz correction according to the analytical expression in Eq. (4) [18] was applied to the *sum*-PED data to obtain the Lorentz corrected *sum*-PED data. All Nb atoms could be located from the projected electrostatic potential map obtained by direct methods from each of the intensity data sets of *sum*-PED, Lorentz corrected *sum*-PED, *max*-PED and *integrated*-PED, although the potential maps are of different quality (Fig. 8 and Supporting information Fig. S1). The worse map is that from the *sum*-PED data and the best

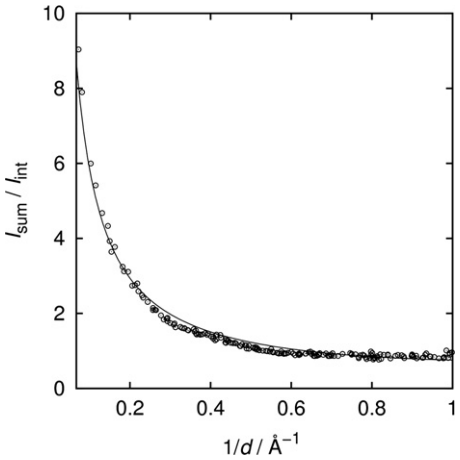

Fig. 7. Ratio of integrated intensity extracted from *sum*-PED and *integrated*-PED patterns. The solid line represents the correction function proposed by Gjønnes [18]. Only reflections with $I > 0.03\ I_{max}$ were used to calculate the intensity ratio in order to minimize the effects of noise.

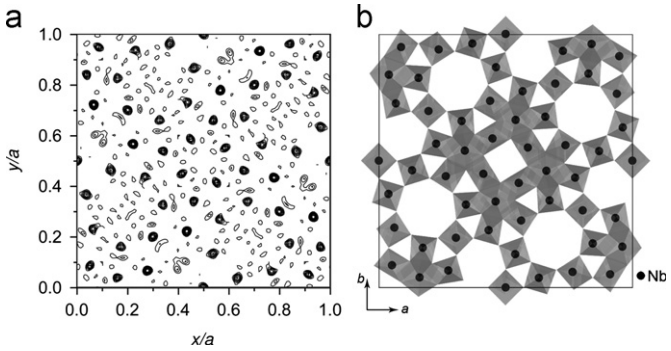

Fig. 8. (a) Projected electrostatic potential map obtained by direct methods using intensities extracted from the *integrated*-PED pattern. (b) The structure model of $K_2O \cdot 7Nb_2O_5$ viewed along the short ***c***-axis.

Table 1
Results of structure refinement on PED data collected at 1.1° precession angle with different data processing strategies. All 305 unique reflections between 15.0 and 1.0 Å resolution are used. They are all observed with $I > 2\,\sigma(I)$ in the case of the *sum*-PED, *integrated*-PED and Lorentz-corrected *sum*-PED data. The *max*-PED data contains 291 reflections with $I > 2\,\sigma(I)$. $\langle \Delta r \rangle$ is the average shift of the Nb positions with respect to the positions in the reference structure [23].

Data set	*sum*-PED	*max*-PED	*integrated*-PED	Lorentz-corrected *sum*-PED
R_{merge}	5.5%	7.5%	12.1%	6.5%
$R1$ (all)	25.1%	27.8%	19.7%	18.8%
$\langle \Delta r \rangle$/Å	0.07(4)	0.07(4)	0.06(3)	0.04(3)

maps are those from the Lorentz corrected *sum*-PED and *integrated*-PED data, which are in fact very similar (Fig. S1).

Three indicators are then used to assess the data quality: (i) the R value for merging symmetry-equivalent reflections, R_{merge}, (ii) the R value for the crystal structure refinement, $R1$ and (iii) the average shift $\langle \Delta r \rangle$ of refined atomic positions compared to the atomic positions from the reference model, i.e. the isostructural $Tl_2O \cdot 7Nb_2O_5$ solved by X-ray crystallography [23]. R_{merge} allows judging the intrinsic data quality, such as statistical intensity variations between equivalent reflections, but also deviations from the zone axis. The remaining two indicators, $R1$ and $\langle \Delta r \rangle$, allow judging the fitness of the data set for electron crystallography, or, more specifically, for crystal structure refinement. Assuming that the structural model is correct, $R1$ measures precision and $\langle \Delta r \rangle$ measures accuracy. Results of structure refinement on PED data for different data processing strategies are summarized in Table 1. R_{merge} is lower than 10% for both *sum*-PED and *max*-PED data, indicating sufficiently high data quality for structure refinement. The R_{merge} of the *integrated*-PED data is larger, which may be caused by slight misalignment of the crystal: even a slight misalignment of the crystal will lead to wrong estimates of the excitation error in the ED frames, especially for the high-resolution reflections. This error will in turn lead to errors in the integrated intensities. If the misalignment is small, it will not show up in the *sum*-PED and max-PED data, because neither the sum nor the maximum of a reflection is influenced as long as the Ewald sphere sweeps through the reflection. While structure refinement on *max*-PED data resulted in slightly larger $R1$ (27.8%) compared to *sum*-PED data (25.1%), significantly smaller $R1$ values (19.7%) are observed for refinements on *integrated*-PED data. However, $\langle \Delta r \rangle$ is almost the same for the three data sets, about 0.07 Å. Refinement using the *integrated*-PED data gives a slightly smaller $\langle \Delta r \rangle$ and a smaller uncertainty in the Nb positions. Even lower $R1$ values (18.8%) were achieved by applying a Lorentz-correction to the *sum*-PED data, which also improved $\langle \Delta r \rangle$. Lorentz-correction of *sum*-PED data leads to an intensity distribution close to that of integrated-PED data, but it is free from errors arising from wrong estimates of the excitation error caused by a slight misalignment of the crystal.

It should be mentioned that the crystal of $K_2O \cdot 7Nb_2O_5$ used here has one short (< 4 Å) axis and a mirror plane perpendicular to the short axis. In such special cases (which are not uncommon among metal oxides), all atoms have to be located exactly in one of the two mirror planes that cut each unit cell at $z = 0$ and $z = ½$. A very large fraction of all the unique diffraction data is then collected in a single projection along that short axis, from which the positions of heavy metal atoms can be found. In a general case, where all unit cell dimensions are larger than 5 Å, it is necessary to collect several zone axes or ideally complete 3D data sets. This can be achieved by electron diffraction tomography [27] or the rotation method [28].

5. Conclusions

We have presented a new software-based precession electron diffraction method, the digital sampling method. The alignment and calibration of the TEM coils for electron beam precession and data collection are completely controlled by software, which replaces the hardware precession devices on a TEM. All the above mentioned procedures are automatic, which simplify the operation procedure and save operation time. The alignment result is often better than what a skillful operator can achieve. By the sampling method, information about the shape of a reflection, which is lost in the conventional PED pattern, is preserved. The digital sampling method provides data for reconstructing the intensity profile of a reflection, and allows performing various data processing procedures. The intensity profile of a reflection may be used for an estimation of the crystal thickness, for studies of diffuse scattering or as a parameter for dynamical structure refinement. The Lorentz effect is effectively corrected in *integrated*-PED data. The intensities extracted from the PED data using different data processing procedures could all be used for partial structure solution and refinement of the $K_2O \cdot 7Nb_2O_5$ crystal. The best results were from the *integrated*-PED ($R1 = 19.7\%$) and the Lorentz-corrected *sum*-PED ($R1 = 18.8\%$). We think this development is just one of the many new possibilities arising, now that computer controlled electron microscopes and detectors are becoming available.

Acknowledgements

The project is supported by the Swedish Research Council (VR), the Swedish Governmental Agency for Innovation Systems (VINNOVA) and the Göran Gustafsson Foundation. The electron microscopes used in this study were purchased from a grant by the Knut and Alice Wallenberg Foundation. W. Wan is supported by a postdoctoral grant from Carl-Trygger Foundation.

Appendix A. Supplementary materials

Supplementary data associated with this article can be found in the online version at doi:10.1016/j.ultramic.2010.09.008.

References

[1] R. Vincent, P.A. Midgley, Ultramicroscopy 53 (1994) 271–282.
[2] J. Gjønnes, V. Hansen, B.S. Berg, P. Runde, Y.F. Cheng, C.J. Gilmore, D.L. Dorset, Acta Crystallogr. A 54 (1998) 306–319.
[3] M. Gemmi, G. Calestani, A. Migliori, Advances in imaging and electron physics, in: P.W. Hawkes, P.G. Merli, G. Calestani, M. Vittori- Antisari (Eds.), Microscopy, Spectroscopy, Holography and Crystallography with Electrons, Vol. 123, Academic Press2002, pp. 311–325.
[4] C.S. Own, A.K. Subramanian, L.D. Marks, Microsc. Microanal. 10 (2004) 96–104.
[5] NanoMEGAS. ⟨http://www.nanomegas.com/⟩.
[6] T.E. Weirich, J. Portillo, G. Cox, H. Hibst, S. Nicolopoulos, Ultramicroscopy 106 (2006) 164–175.
[7] K. Boulahya, L. Ruiz-González, M. Parras, J.M. Gonza lez-Calbet, M.S. Nickolsky, S. Nicolopoulos, Ultramicroscopy 107 (2007) 445–452.
[8] D.L. Dorset, C.J. Gilmore, J.L. Jorda, S. Nicolopoulos, Ultramicroscopy 107 (2007) 462–473.
[9] A. Kverneland, V. Hansen, R. Vincent, K. Gjønnes, J. Gjønnes, Ultramicroscopy 106 (2006) 492–502.
[10] M. Gemmi, S. Nicolopoulos, Ultramicroscopy 107 (2007) 483–494.
[11] E. Mugnaioli, T. Gorelik, U. Kolb, Ultramicroscopy 109 (2009) 758–765.
[12] P. Boullay, V. Dorcet, O. Pérez, C. Grygiel, W. Pellier, B. Mercey, M. Hervieu, Phys. Rev. B 79 (2009) 184108.
[13] M. Gemmi, H. Klein, A. Rageau, P. Strobel, F.Le Cras, Acta Crystallogr. B66 (2010) 60–68.
[14] L. Kienle, V. Smetana, V. Duppel, A. Simon, Z. Anorg. Allg. Chem. 636 (2010) 325–330.
[15] T.A. White, M.S. Moreno, P.A. Midgley, Z. Kristallogr. 225 (2010) 56–66.
[16] J.P. Morniroli, A. Redjaïmia, Ultramicroscopy 107 (2007) 514–522.
[17] J.P. Morniroli, A. Redjaimia, Journal of Microscopy 227 (2007) 157–171.
[18] K. Gjønnes, Ultramicroscopy 69 (1997) 1–11.

[19] A. Avilov, K. Kuligin, S. Nicolopoulos, M. Nickolskiy, K. Boulahyad, J. Portillo, G. Lepeshov, B. Sobolev, J.P. Collette, N. Martin, A.C. Robins, P. Fischione, Ultramicroscopy 107 (2007) 431–444.
[20] C.T. Koch, P. Bellina, P.A. van Aken, 14th European microscopy congress (EMC), vol. 2: Materials Science, Springer, Berlin Heidelberg, 2008 p.201–202.
[21] J.J. Hu, F.H. Li, H.F. Fan, Ultramicroscopy 41 (1992) 387–397.
[22] P. Oleynikov, D. Grüner, D. Zhang, J. Sun, X.D. Zou, S. Hovmöller, in: P. Moeck, S. Hovmoeller, S. Nicolopoulos, S. Rouvimov, V. Petkov, M. Gateshki, P. Fraundorf (Eds.), Electron Crystallography for Materials Research and Quantitative Characterization of Nanostructured Materials, Mater. Res. Soc. Symp. Proc., Vol. 1184, Warrendale, PA. (2009), 1–4.
[23] V. Bhide, M. Gasparin, Acta Crystallogr. B 35 (1979) 1318–1321.
[24] X.D. Zou, Y. Sukharev, S. Hovmöller, Ultramicroscopy 49 (1993) 147–158.
[25] Calidris. 〈http://www.calidris-em.com/〉.
[26] G.M. Sheldrick, Acta Crystallogr. A 64 (2008) 112–122.
[27] U. Kolb, T. Gorelik, C. Kübel, M.T. Otten, D. Hubert, Ultramicroscopy 107 (2007) 507–513.
[28] D.L. Zhang, P. Oleynikov, S. Hovmöller, X.D. Zou, Z. Kristallogr. 225 (2010) 94–102.